Mechanical twinning of monazite expels radiogenic lead

D. Fougerouse[1,2]*, S.M. Reddy[1,2], A.-M. Seydoux-Guillaume[3,4], C.L. Kirkland[5], T.M. Erickson[1,6], D.W. Saxey[2], W.D.A. Rickard[2], D. Jacob[7], H. Leroux[7] and C. Clark[1]

[1]School of Earth and Planetary Sciences, Curtin University, Perth, Western Australia 6845, Australia
[2]Geoscience Atom Probe, John de Laeter Centre, Curtin University, Perth, Western Australia 6845, Australia
[3]Université de Lyon, CNRS, UCBL, ENSL, LGL-TPE, 69622 Villeurbanne, France
[4]Université de Lyon, Université Jean Monnet-Saint-Etienne, F-42023 Saint-Etienne, France
[5]School of Earth and Planetary Sciences, Centre for Exploration Targeting–Curtin Node, Curtin University, Perth, Western Australia 6845, Australia
[6]Jacobs–JETS, Astromaterials Research and Exploration Science Division, National Aeronautics and Space Administration Johnson Space Center, Houston, Texas 77058, USA
[7]UMET–Unité Matériaux et Transformations, Université de Lille, CNRS, INRAE, Centrale Lille, UMR 8207, F-59000 Lille, France

ABSTRACT

Mechanical twins form by the simple shear of the crystal lattice during deformation. In order to test the potential of narrow twins in monazite to record the timing of their formation, we investigated a ca. 1700 Ma monazite grain (from the Sandmata Complex, Rajasthan, India) deformed at ca. 980 Ma, by electron backscattered diffraction (EBSD), transmission electron microscopy (TEM), and atom probe tomography (APT). APT $^{208}Pb/^{232}Th$ ages indicate that the twin was entirely reset by radiogenic Pb loss during its formation at conditions far below the monazite closure temperature. The results are consistent with a model where Pb is liberated during rupture of rare earth element–oxygen (REE-O) bonds in the large $[REE]O_9$ polyhedra during twinning. Liberated Pb likely migrated along fast diffusion pathways such as crystal defects. The combination of a quantitative microstructural investigation and nanogeochronology provides a new approach for understanding the history of accessory phases.

INTRODUCTION

The radiogenic decay of U and Th into different isotopes of Pb enables a series of widely used geochronometers. Critical to this application is an understanding of the mobility of radiogenic Pb in minerals and how this underpins our ability to use and develop U-Th-Pb geochronology. Traditional models for Pb mobility assume temperature-dependent volume diffusion of Pb through the crystal lattice of the mineral. More recently, a number of studies have reported a relationship between trace element mobility and deformation (Moser et al., 2009; Timms et al., 2011; Piazolo et al., 2012; Reddy et al., 2016; Kirkland et al., 2018; Fougerouse et al., 2019). Pb mobility has been suggested to occur in high-closure-temperature minerals (zircon and monazite) during crystal-plastic deformation (Moser et al., 2009) and deformation-induced grain boundary migration (Erickson et al., 2015), with radiogenic Pb accumulation continuing after deformation.

Deformation twinning is a common, narrow (<3 µm) microstructural feature in deformed minerals and forms by the simple shear of the crystal lattice and a highly ordered displacement of atoms. Twinning is sensitive to temperature during deformation and to strain rate, and typically is more dominant than slip at lower temperatures or at higher strain rates (Christian and Mahajan, 1995). Mechanical twinning is a deformation microstructure that has found use as a geothermometer in calcite (Ferrill et al., 2004) and as a tool to determine compressive stress direction (Jamison and Spang, 1976), and has been considered a diagnostic microstructure for impact-related deformation in quartz, zircon, and monazite (Goltrant et al., 1992; Moser et al., 2011; Timms et al., 2012; Erickson et al., 2016b).

In this study, we integrate electron backscattered diffraction (EBSD), transmission electron microscopy (TEM), and atom probe tomography (APT) analyses to investigate Pb mobility associated with micrometer-scale deformation twins formed within tectonically deformed monazite.

We provide a framework for the analysis of mineral twins in monazite that could be further utilized in the analysis of nanoscale microstructural features in other accessory phases.

SAMPLES AND METHODOLOGY

We re-investigated a monazite grain from the granulite-facies rocks of the Sandmata Complex, Rajasthan, India (Fig. 1), which was previously studied in detail by Erickson et al. (2015) and Fougerouse et al. (2018). Two high-temperature metamorphic events are recognized in this region: a first event at ca. 1720 Ma (event $M1_{SC}$; ~700–1000 MPa and 800–900 °C), which resulted in growth of the original monazite; and a second, fluid-absent event at ca. 1000 Ma (event $M2_{SC}$; ~500–700 MPa and 600–750 °C; Buick et al., 2006). EBSD and secondary ion mass spectrometry (SIMS) U-Pb analyses reveal partial Pb loss in deformed domains of monazite and growth of neoblasts at 970 ± 14 Ma (2σ, $n = 6$, mean squared weighted deviation [MSWD] = 1.3; Erickson et al., 2015). Due to a spot size larger that the mechanical twins, SIMS analyses of mixed twin and host domains yield imprecise U-Pb discordant data, implying partial Pb loss in the domain analyzed. These mixed domains could not be used to successfully constrain the timing of monazite deformation (Erickson et al., 2015).

The EBSD analyses were used to investigate crystal lattice orientation variations and were conducted on a Tescan Mira3 scanning electron microscope equipped with a Nordlys Nano high-resolution detector at Curtin University (Perth, Australia). Details of the EBSD analyses are given by Erickson et al. (2015).

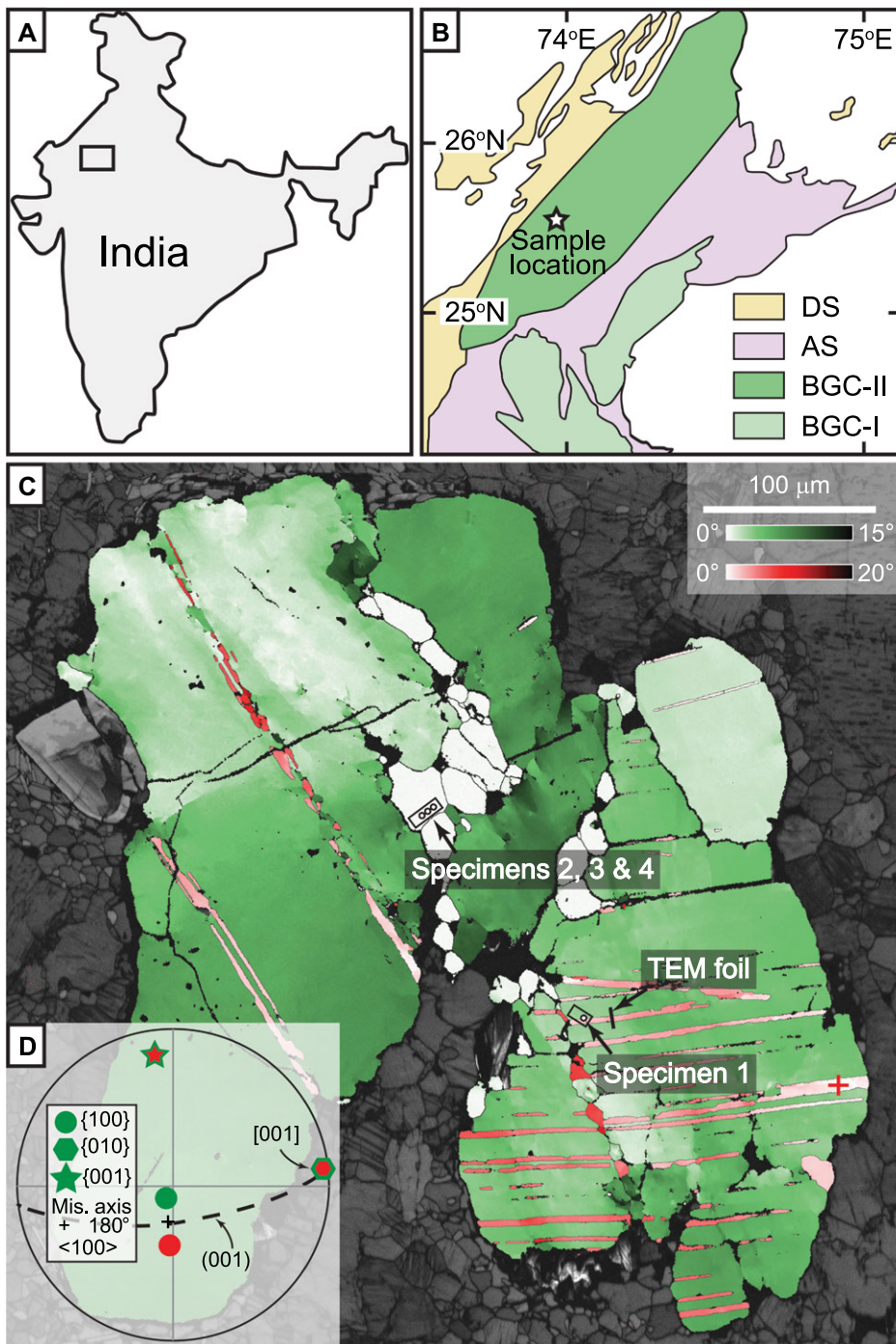*E-mail: denis.fougerouse@curtin.edu.au

Figure 1. (A) Boundary map of India (box shows location of B). (B) Simplified geological map of the Sandmata granulite complex (modified from Buick et al., 2006), with location of our monazite grain sample. DS—Delhi Supergroup; AS—Aravalli Supergroup; BGC-II—Archean banded gneiss complex; BGC-I—Proterozoic banded gneiss complex. (C) Crystallographic orientation electron backscattered diffraction map. Grain reference orientation deviation up to 15° is shown via the green color scale; twins are color-coded red for misorientation ranging between 0° and 20° from the reference point "+"; modified from Erickson et al. (2015). Atom probe tomography (APT) samples were extracted from a (100) twin (specimen 1) and one neoblast (specimens 2, 3, and 4). TEM—transmission electron microscopy. (D) Lower-hemisphere, equal-area projection of crystal orientation data at the site of APT specimen 1. Green symbols represent monazite host; red symbols are twin domain. Mis.—misorientation.

same instrument across the boundary between the twin and the monazite host (Fig. 1C) and further thinned using a FEI Helios 600i FIB-SEM (Manutech-USD, Saint-Etienne, France).

The TEM foil was studied using a FEI Titan Themis 300 (Université de Lille, France) to obtain high-resolution high-angle annular dark field (HR-HAADF) images and energy dispersive X-ray spectroscopy (EDS) with a Super-X windowless, four-quadrant silicon drift detector (SDD) in scanning transmission electron microscope (STEM) mode.

The APT analyses were performed on a Cameca LEAP 4000X HR at the Geoscience Atom Probe facility at Curtin University (Reddy et al., 2020). The instrument was operated in laser pulsed mode with a UV laser ($\lambda = 355$ nm), laser pulse energy of 100 pJ, base temperature of 50 K, and automated detection rate of 0.01 atoms per pulse. Four data sets were collected with ~8, 26, 27, and 40×10^6 atoms, respectively. The $^{208}Pb/^{232}Th$ age was measured using the $^{208}Pb^{2+}$ and $^{232}ThO^{2+}$ signal and corrected following the protocol defined by Fougerouse et al. (2020). Counts were quantified by subtracting the estimated background counts from each peak. The local background level was measured from the counts in a nearby "peak-free" range and normalized to the width of the range used for quantification (0.1 Da). The isotopic ratio uncertainties are derived from the uncertainty of each species used for calculating the ratio and reported at 95% confidence (2σ). The linear correlation [$y = 0.381(\pm0.048)x - 254(\pm26)$] between the $^{208}Pb/^{232}Th$ fractionation coefficient (y) and the $M/\Delta M_{10}$ peak parameter (x), where M is the position of the O_2^+ peak and ΔM_{10} its full width at tenth maximum, was used to correct for molecular fractionation and calculate $^{208}Pb/^{232}Th$ ages (Fougerouse et al., 2020). The error propagation of the prediction is derived from the uncertainty of the $M/\Delta M_{10}$ value, the uncertainty of the measured $^{208}Pb/^{232}ThO$ ratio, and the 95% prediction band.

RESULTS

The EBSD data show that the twin is crystallographically equivalent to a 180° rotation about <100>, consistent with apparent shearing in the [100] direction on the (001) plane (e.g., Erickson et al., 2016b). The observed twin dimensions in the plane of the thin section are ~80 μm long and 2.5 μm wide. Both the twin domain and the host monazite are relatively undeformed in the region sampled for APT, with a maximum of 3.5° cumulative misorientation.

The APT results of specimen 1 (twin) reveal that the Ca distribution is heterogeneous within two distinct compositional domains separated by the twin boundary (Fig. 2). A proportion of the Ca within the host is clustered along with Si and Pb (~10 at% Ca, ~1
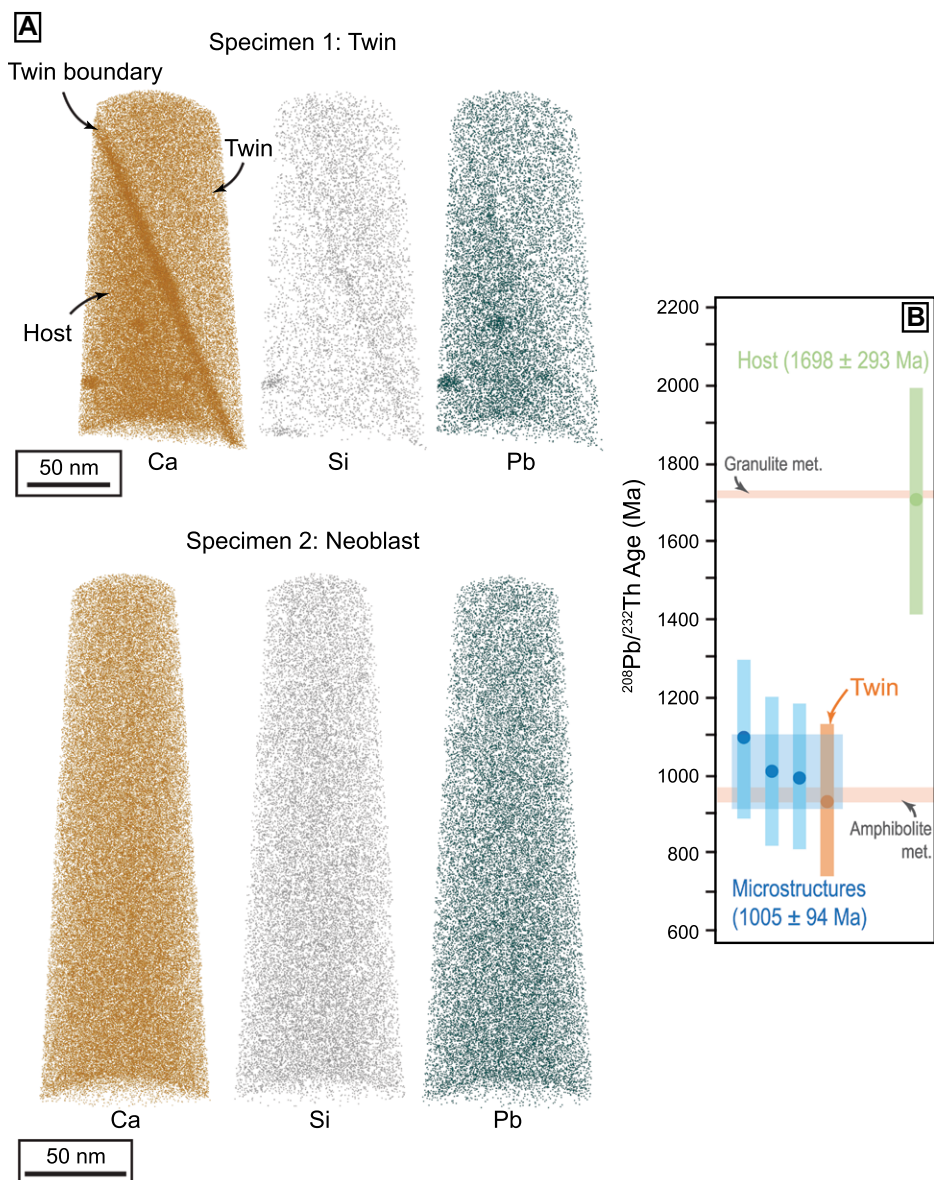
One APT specimen was prepared from a (001) twin (specimen 1) and three specimens from a neoblast (specimens 2–4) by focused ion beam–scanning electron microscopy (FIB-SEM; Fig. 1C). A Tescan Lyra3 Ga+ FIB-SEM was used to produce needle specimens and precisely select the specimen location (Rickard et al., 2020). A TEM foil was prepared with the

Figure 2. (A) Reconstructed three-dimensional atom probe image of Ca, Si, and 208Pb distribution for specimen 1 (twin and host) and specimen 2 (neoblast) from the studied monazite grain (Sandmata Complex, Rajasthan, India). Each sphere represents one atom. The twinned domain is marked by homogeneous Ca, Si, and Pb distribution, whereas the host is heterogeneous with apatite nano-inclusions. Neoblast Ca, Si, and Pb distribution is homogeneous. (B) Nanoscale $^{208}Pb/^{232}Th$ age data. Ages are color coded by grain domains (green—host; blue—neoblast; orange—twin). Blue box represents weighted mean age of the neoblast and twinned domains at 2σ uncertainty. Host monazite age is consistent with granulite metamorphism (met.) event, whereas neoblast and twin ages are consistent with deformation associated with amphibolite metamorphism.

at% Si and ~0.7 at% Pb), consistent with nanoscale inclusions of apatite in other APT studies of monazite (Fougerouse et al., 2018), whereas the twin appears homogeneous. The trace element compositions of the host and the twin are dissimilar, with higher Ca and Pb (1.1 versus 0.8 at% Ca and 0.09 versus 0.05 at% Pb, respectively) and lower Si concentration in the host (0.04 versus 0.1 at% Si, respectively). The twin boundary separating these two domains is enriched in Ca (2.3 at%) and Si (0.3 at%), weakly enriched in Pb (only visible in three-dimensional atom maps; Fig. 2), and depleted in rare earth elements (REEs) and phosphorus (P).

The APT $^{208}Pb^{2+}/^{232}ThO^{2+}$ ratio of the host, including the clusters, is 0.1789 ± 0.0058, whereas the twin-domain $^{208}Pb^{2+}/^{232}ThO^{2+}$ ratio is 0.0965 ± 0.0057 (2σ; Fig. 2). The peak parameter $M/\Delta M_{10}$ for this specimen is 533.8 ± 2.7. Fractionation-corrected APT $^{208}Pb/^{232}Th$ age for the host domain of specimen 1 is 1698 ± 293 Ma (2σ), whereas the twin domain of specimen 1 yields an age of 934 ± 193 Ma. The APT re-

sults from specimens 2, 3, and 4 from a single neoblast are consistent across all specimens, with homogenous distribution of major and trace elements (Fig. 2; Fig. S1 in the Supplemental Material[1]). In the neoblasts, the APT $^{208}Pb^{2+}/^{232}ThO^{2+}$ ratio is 0.1074 ± 0.0048 for specimen 2, 0.1117 ± 0.0056 for specimen 3, and 0.1039 ± 0.0048 for specimen 4. The peak parameter $M/\Delta M_{10}$ is 530.2 ± 1.7 for specimen 2, 535.8 ± 1.8 for specimen 3, and 532.5 ± 1.8 for specimen 4, yielding corrected ages of 1008 ± 198 Ma, 1093 ± 204 Ma, and 994 ± 186 Ma, respectively (Fig. 2). The ages of the twinned domain and neoblast are within uncertainty of each other and have a weighted mean average of 1005 ± 94 Ma (2σ).

A HR-HAADF image across the twin boundary indicates the absence of an amorphous film, and it is semi-coherent (Fig. 3B; Ranganathan, 1966). The STEM-EDS results are consistent with the APT findings, with enrichment in Ca and depletions in light REEs and P within only a few nanometers of the boundary (Fig. S2).

AGE RESETTING AND Pb MOBILITY DURING TWIN FORMATION

The APT $^{208}Pb/^{232}Th$ ages are in good agreement with previously published SIMS and electron microprobe data for the metamorphic history of the region (Buick et al., 2006; Erickson et al., 2015). The age of the monazite host corresponds to the timing of granulite-facies metamorphism that affected the region at 1720 ± 10 Ma (Buick et al., 2006). The 1005 ± 94 Ma weighted mean age obtained for recrystallized neoblasts and the twinned domain in specimen 1 is consistent (within uncertainty) with a 970 ± 14 Ma amphibolite-facies metamorphism and regional deformation event (Buick et al., 2006; Erickson et al., 2015). Therefore, all radiogenic and initial Pb was expelled from the twinned domain of the monazite crystal during the deformation event (Fig. 4).

Twin nucleation and growth have been extensively explored in the material sciences literature (Christian and Mahajan, 1995; Beyerlein et al., 2014). Mechanical twins are formed by the simple shear of the crystal lattice and the continuous movement of partial dislocations; however, no studies have previously shown a relationship between twin formation and the resetting of the Th-Pb chronometer.

Three possible mechanisms can explain the resetting of the twinned domain: (1) dynamic recrystallization during metamorphism, (2) fluid alteration replacement, and (3) Pb
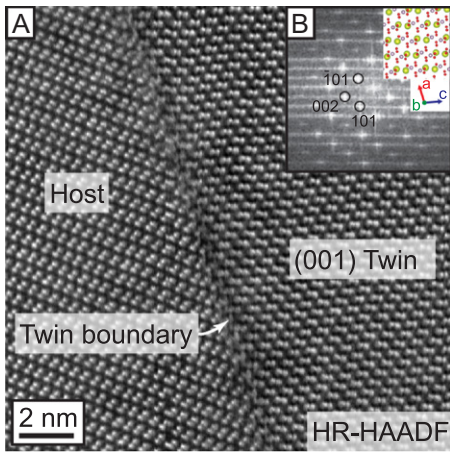
Figure 3. (A) High-resolution high-angle annular dark field (HR-HAADF) image of twin boundary, showing the absence of amorphous material within the boundary. (B) Indexed Fourier transform of the square area on the right side of the HR-HAADF image and the structure model seen along [010] orientation. Red spheres represent oxygen atoms, purple spheres represent Pb atoms, and yellow spheres represent rare earth element (REE) atoms. Only heavy REE atoms are seen on the HR-HAADF image.

liberation during crystal shearing. The studied twin is weakly deformed (as much as 3.5° of cumulative misorientation), is a single 80-μm-long domain, and lacks triple junctions. These observations suggest that the twin did not recrystallize after formation. We postulate that fluid-assisted recrystallization (i.e., pressure solution) did not operate during deformation of the Sandmata monazite based on the lack of a free, interconnected fluid phase in the lower crust (Yardley and Valley, 1997), coupled with textural evidence including the isolation of strain-free neoblasts within the grain interior and the absence of resetting along the exterior of the monazite (Erickson et al., 2015, 2016a). In addition, high-resolution TEM data indicate that the host and the twin have a semi-coherent boundary, unavailable to fluid infiltration (Fig. 3). The role of a small amount of fluid (H_2O, CO_2) at the grain boundary is difficult to assess but may have been to facilitate the reactive transports of ions to and from the crystal surface. Therefore, we favor the third mechanism.

In monazite, Ca^{2+}, Th^{4+}, and U^{4+} reside within the REE sites (Ni et al., 1995), and radiogenic Pb^{2+} is repositioned in the monazite crystal structure on the REE sites after alpha recoil during self-annealing (Seydoux-Guillaume et al., 2018; Tang et al., 2020). The monazite crystal structure is composed of an arrangement of small PO_4 tetrahedra (P-O bond lengths of 0.1524–0.1540 nm) and larger $[REE]O_9$ polyhedra (REE-O bond lengths of 0.250–0.277 nm). These crystal lattice parameters suggest that the PO_4 tetrahedra are more rigid compared to

the $[REE]O_9$ polyhedra and that REE-O bonds are more likely to break than P-O bonds during twinning (Hay and Marshall, 2003). This preferential point of rupture would also affect radiogenic Pb-O and Ca-O bonds because they share the same sites, and potentially release Pb and Ca during this process (Fig. 4). The prediction of this model is that the liberation of Ca and Pb would result in a Pb-Ca–free twinned domain and the accumulation of Ca and Pb within the twin boundary. The nanogeochronology data indicate that all of the radiogenic Pb was mobilized during twin formation, while Ca composition changed by ~25%, from 1.1 at% in the host to 0.8 at% in the twinned domain. Ca is also highly enriched in the twin boundary (as much as 2.3 at%) whereas Pb is weakly concentrated in the same domain, indicating that different mechanisms may affect Pb and Ca liberation during crystal shearing. In ninefold coordination, the ionic radius of Pb^{2+} (1.35 Å) is larger than that of Ca^{2+} (1.18 Å; Shannon, 1976). During twinning, dislocations are necessary at the point of shearing (Cottrell and Bilby, 1951). Dislocations can trap impurities in the distorted crystal lattice surrounding the dislocation (Cottrell and Bilby, 1949) or in their cores (Johnston and Gilman, 1959). Large ions such as Pb^{2+} are likely hosted in the core of the dislocation, as opposed to smaller ions such as Ca^{2+} more suited to the locally distorted lattice. Ions in dislocation cores can diffuse faster along the linear defect (Love, 1964), allowing for an efficient expulsion of Pb compared to Ca. A portion of the Ca in the distorted crystal lattice surrounding the dislocation may be reincorporated in the twinned domain as the shearing of the crystal progresses or upon subsequent thermal annealing.
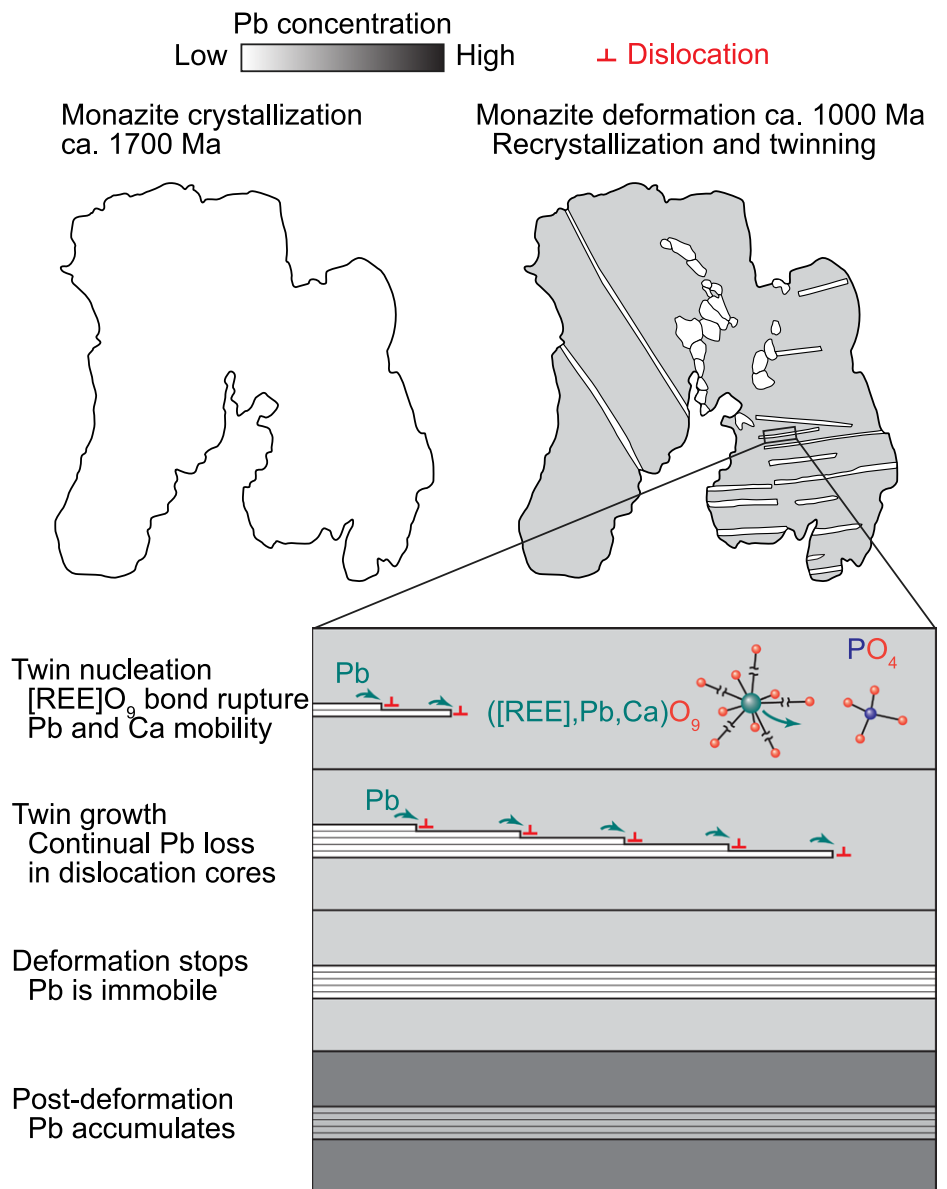

Figure 4. Schematic model of age resetting of the studied twin during its formation. Diagram is not at scale.

No experimental data are available to constrain the temperature dependency of Pb diffusion along crystal defects, and the influence of temperature and strain rate on Pb isotopic resetting is uncertain. Nonetheless, this study demonstrates that Pb is mobilized by twin formation during deformation at 600 °C. We highlight that this approach offers the potential to temporally constrain larger-scale processes, including tectonic and shock-driven metamorphism, the ages of which have hitherto remained elusive.

REFERENCES CITED
Beyerlein, I.J., Zhang, X., and Misra, A., 2014, Growth twins and deformation twins in metals: Annual Review of Materials Research, v. 44, p. 329–363, https://doi.org/10.1146/annurev-matsci-070813-113304.

Buick, I.S., Allen, C., Pandit, M., Rubatto, D., and Hermann, J., 2006, The Proterozoic magmatic and metamorphic history of the Banded Gneiss Complex, central Rajasthan, India: LA-ICP-MS U-Pb zircon constraints: Precambrian Research, v. 151, p. 119–142, https://doi.org/10.1016/j.precamres.2006.08.006.

Christian, J.W., and Mahajan, S., 1995, Deformation twinning: Progress in Materials Science, v. 39, p. 1–157, https://doi.org/10.1016/0079-6425(94)00007-7.

Cottrell, A.H., and Bilby, B.A., 1949, Dislocation theory of yielding and strain ageing of iron: Proceedings of the Physical Society: Section A, v. 62, p. 49–62, https://doi.org/10.1088/0370-1298/62/1/308.

Cottrell, A.H., and Bilby, B.A., 1951, A mechanism for the growth of deformation twins in crystals: The London, Edinburgh, and Dublin Philosophical Magazine and Journal of Science, Ser. 7, v. 42, p. 573–581, https://doi.org/10.1080/14786445108561272.

Erickson, T.M., Pearce, M.A., Taylor, R.J.M., Timms, N.E., Clark, C., Reddy, S.M., and Buick, I.S., 2015, Deformed monazite yields high-temperature tectonic ages: Geology, v. 43, p. 383–386, https://doi.org/10.1130/G36533.1.

Erickson, T.M., Reddy, S.M., Timms, N.E., Pearce, M.A., Taylor, R.J.M., Clark, C., and Buick, I.S., 2016a, Deformed monazite yields high-temperature tectonic ages: Reply: Geology, v. 44, p. e378, https://doi.org/10.1130/G37474Y.1.

Erickson, T.M., Cavosie, A.J., Pearce, M.A., Timms, N.E., and Reddy, S.M., 2016b, Empirical constraints on shock features in monazite using shocked zircon inclusions: Geology, v. 44, p. 635–638, https://doi.org/10.1130/G37979.1.

Ferrill, D.A., Morris, A.P., Evans, M.A., Burkhard, M., Groshong, R.H., Jr., and Onasch, C.M., 2004, Calcite twin morphology: A low-temperature deformation geothermometer: Journal of Structural Geology, v. 26, p. 1521–1529, https://doi.org/10.1016/j.jsg.2003.11.028.

Fougerouse, D., Reddy, S.M., Saxey, D.W., Erickson, T.M., Kirkland, C.L., Rickard, W.D.A., Seydoux-Guillaume, A.-M., Clark, C., and Buick, I.S., 2018, Nanoscale distribution of Pb in monazite revealed by atom probe microscopy: Chemical Geology, v. 479, p. 251–258, https://doi.org/10.1016/j.chemgeo.2018.01.020.

Fougerouse, D., Reddy, S.M., Kirkland, C.L., Saxey, D.W., Rickard, W.D., and Hough, R.M., 2019, Time-resolved, defect-hosted, trace element mobility in deformed Witwatersrand pyrite: Geoscience Frontiers, v. 10, p. 55–63, https://doi.org/10.1016/j.gsf.2018.03.010.

Fougerouse, D., Kirkland, C.L., Saxey, D.W., Seydoux-Guillaume, A.-M., Rowles, M.R., Rickard, W.D.A., and Reddy, S.M., 2020, Nanoscale isotopic dating of monazite: Geostandards and Geoanalytical Research, https://doi.org/10.1111/ggr.12340 (in press).

Goltrant, O., Leroux, H., Doukhan, J.-C., and Cordier, P., 1992, Formation mechanisms of planar deformation features in naturally shocked quartz: Physics of the Earth and Planetary Interiors, v. 74, p. 219–240, https://doi.org/10.1016/0031-9201(92)90012-K.

Hay, R.S., and Marshall, D.B., 2003, Deformation twinning in monazite: Acta Materialia, v. 51, p. 5235–5254, https://doi.org/10.1016/S1359-6454(03)00305-7.

Jamison, W.R., and Spang, J.H., 1976, Use of calcite twin lamellae to infer differential stress: Geological Society of America Bulletin, v. 87, p. 868–872, https://doi.org/10.1130/0016-7606(1976)87<868:UOCTLT>2.0.CO;2.

Johnston, W.G., and Gilman, J.J., 1959, Dislocation velocities, dislocation densities, and plastic flow in lithium fluoride crystals: Journal of Applied Physics, v. 30, p. 129–144, https://doi.org/10.1063/1.1735121.

Kirkland, C.L., Fougerouse, D., Reddy, S.M., Hollis, J., and Saxey, D.W., 2018, Assessing the mechanisms of common Pb incorporation into titanite: Chemical Geology, v. 483, p. 558–566, https://doi.org/10.1016/j.chemgeo.2018.03.026.

Love, G.R., 1964, Dislocation pipe diffusion: Acta Metallurgica, v. 12, p. 731–737, https://doi.org/10.1016/0001-6160(64)90220-2.

Moser, D.E., Davis, W.J., Reddy, S.M., Flemming, R.L., and Hart, R.J., 2009, Zircon U-Pb strain chronometry reveals deep impact-triggered flow: Earth and Planetary Science Letters, v. 277, p. 73–79, https://doi.org/10.1016/j.epsl.2008.09.036.

Moser, D.E., Cupelli, C.L., Barker, I.R., Flowers, R.M., Bowman, J.R., Wooden, J., and Hart, J.R., 2011, New zircon shock phenomena and their use for dating and reconstruction of large impact structures revealed by electron nanobeam (EBSD, CL, EDS) and isotopic U-Pb and (U-Th)/He analysis of the Vredefort dome: Canadian Journal of Earth Sciences, v. 48, p. 117–139, https://doi.org/10.1139/E11-011.

Ni, Y., Hughes, J.M., and Mariano, A.N., 1995, Crystal chemistry of the monazite and xenotime structures: American Mineralogist, v. 80, p. 21–26, https://doi.org/10.2138/am-1995-1-203.

Piazolo, S., Austrheim, H., and Whitehouse, M., 2012, Brittle-ductile microfabrics in naturally deformed zircon: Deformation mechanisms and consequences for U-Pb dating: American Mineralogist, v. 97, p. 1544–1563, https://doi.org/10.2138/am.2012.3966.

Ranganathan, S., 1966, On the geometry of coincidence-site lattices: Acta Crystallographica, v. 21, p. 197–199, https://doi.org/10.1107/S0365110X66002615.

Reddy, S.M., et al., 2016, Mechanisms of deformation-induced trace element migration in zircon resolved by atom probe and correlative microscopy: Geochimica et Cosmochimica Acta, v. 195, p. 158–170, https://doi.org/10.1016/j.gca.2016.09.019.

Reddy, S.M., Saxey, D.W., Rickard, W.D.A., Fougerouse, D., Montalvo, S.D., Verberne, R., and van Riessen, A., 2020, Atom probe tomography: Development and application to the geosciences: Geostandards and Geoanalytical Research, v. 44, p. 5–50, https://doi.org/10.1111/ggr.12313.

Rickard, W.D.A., Reddy, S.M., Saxey, D.W., Fougerouse, D., Timms, N.E., Daly, L., Peterman, E., Cavosie, A.J., and Jourdan, F., 2020, Novel applications of FIB-SEM-based ToF-SIMS in atom probe tomography workflows: Microscopy and Microanalysis, v. 26, p. 750–757, https://doi.org/10.1017/S1431927620000136.

Seydoux-Guillaume, A.-M., Deschanels, X., Baumier, C., Neumeier, S., Weber, W.J., and Peuget, S., 2018, Why natural monazite never becomes amorphous: Experimental evidence for alpha self-healing: American Mineralogist, v. 103, p. 824–827, https://doi.org/10.2138/am-2018-6447.

Shannon, R.D., 1976, Revised effective ionic radii and systematic studies of interatomic distances in halides and chalcogenides: Acta Crystallographica: Section A, Crystal Physics, Diffraction, Theoretical and General Crystallography, v. 32, p. 751–767, https://doi.org/10.1107/S0567739476001551.

Tang, X., Li, Q.-L., Zhang, B., Wang, P., Gu, L.-X., Ling, X.-X., Fei, C.-H., and Li, J.-H., 2020, The chemical state and occupancy of radiogenic Pb, and crystallinity of RW-1 monazite revealed by XPS and TEM: Minerals (Basel), v. 10, 504, https://doi.org/10.3390/min10060504.

Timms, N.E., Kinny, P.D., Reddy, S.M., Evans, K., Clark, C., and Healy, D., 2011, Relationship among titanium, rare earth elements, U-Pb ages and deformation microstructures in zircon: Implications for Ti-in-zircon thermometry: Chemical Geology, v. 280, p. 33–46, https://doi.org/10.1016/j.chemgeo.2010.10.005.

Timms, N.E., Reddy, S.M., Healy, D., Nemchin, A.A., Grange, M.L., Pidgeon, R.T., and Hart, R., 2012, Resolution of impact-related microstructures in lunar zircon: A shock-deformation mechanism map: Meteoritics & Planetary Science, v. 47, p. 120–141, https://doi.org/10.1111/j.1945-5100.2011.01316.x.

Yardley, B.W., and Valley, J.W., 1997, The petrologic case for a dry lower crust: Journal of Geophysical Research, v. 102, p. 12,173–12,185, https://doi.org/10.1029/97JB00508.

Printed in USA